



1 **Real-time coastal flood hazard assessment using DEM-based**  
2 **hydrogeomorphic classifiers**

3

4

5 Keighobad Jafarzadegan<sup>1</sup>, David F. Muñoz<sup>1</sup>, Hamed Moftakhari<sup>1</sup>, Joseph L Gutenson<sup>2</sup>,  
6 Gaurav Savant<sup>2</sup>, Hamid Moradkhani<sup>1</sup>

7

8 <sup>1</sup> Center for Complex Hydrosystems Research, Department of Civil, Construction, and  
9 Environmental Engineering, University of Alabama, Tuscaloosa, AL

10 <sup>2</sup> US Army Engineer Research and Development Center, Coastal and Hydraulics Laboratory,  
11 Vicksburg, MS, USA

12

13 *Correspondence to:* Keighobad Jafarzadegan [kjafarzadegan@ua.edu](mailto:kjafarzadegan@ua.edu)

14

15 **Key Points**

16• A DEM-based approach is developed for rapid flood hazard assessment in coastal regions.

17• The Height Above Nearest Drainage (HAND) is modified for flood mapping in flat areas.

18• Operative hydrogeomorphic curves are proposed for real-time flood hazard mapping.

19

20

21

22



## 23 **Abstract**

24 Deltas, estuaries, and wetlands are prone to frequent coastal flooding throughout the world. In  
25 addition, a large number of people in the United States have settled in these low-lying regions.  
26 Therefore, the ecological merit of wetlands for maintaining sustainable ecosystems highlights the  
27 importance of flood risk and hazard management in these regions. Typically, hydrodynamic  
28 models are used for coastal flood hazard mapping. The huge computational resources required for  
29 hydrodynamic modeling and the long-running time of these models (order of hours or days) are  
30 two major drawbacks that limit the application of these models for prompt decision-making by  
31 emergency responders. In the last decade, DEM-based classifiers based on Height Above Nearest  
32 Drainage (HAND) have been widely used for rapid flood hazard assessment demonstrating  
33 satisfactory performance for inland floods. The main limitation is the high sensitivity of HAND to  
34 the topography which degrades the accuracy of these methods in flat coastal regions. In addition,  
35 these methods are mostly used for a given return period and generate static hazard maps for past  
36 flood events. To cope with these two limitations, here we modify HAND and propose a composite  
37 hydrogeomorphic index for rapid flood hazard assessment in coastal areas. We also propose the  
38 development of hydrogeomorphic threshold operative curves for real-time flood hazard mapping.  
39 We select the Savannah river delta as a testbed, calibrate the proposed hydrogeomorphic index on  
40 Hurricane Matthew and validate the performance of the developed operative curves for Hurricane  
41 Irma. Validation results demonstrate that the operative curves can rapidly generate flood hazard  
42 maps with satisfactory accuracy. This indicates the high efficiency of our proposed methodology  
43 for fast and accurate estimation of hazard areas for an upcoming coastal flood event which can be  
44 beneficial for emergency responders and flood risk managers.



## 45 **1. Introduction**

46 Densely populated coastal areas are some of the most productive ecosystems on Earth. Coastal  
47 wetlands provide important services to society, including flood attenuation, water storage, carbon  
48 sequestration, nutrient cycling, pollutant removal, and wildlife habitat (Barbier, 2019; Land et al.,  
49 2019; Wamsley et al., 2010). Characterizing the hydrological processes unique to coastal areas is  
50 tremendously important for ensuring the sustainability of these ecosystem services. Endangered  
51 coastal ecosystems are threatened by anthropogenic effects including direct impacts of human  
52 activities (i.e. urbanization and navigational development) or indirect impacts (e.g. sea level rise  
53 (SLR), and hydroclimate extremes exacerbated by climate change (Alizad et al., 2018; Kirwan and  
54 Megonigal, 2013; Wu et al., 2017). Nearly 70% of global wetlands have been lost since the 1900s  
55 and rates of wetland loss have increased by a factor of 4 in the late 20<sup>th</sup> and early 21<sup>st</sup> century  
56 (Davidson, 2014). Urbanization hinders wetland migration toward upland areas in an effort to cope  
57 with rising water levels (WLs) (Schieder et al., 2018). Likewise, moderate to high Relative Sea  
58 Level Rise (RSLR) rates can influence the fate of sediments and nutrient availability to coastal  
59 wetlands (Schile et al., 2014); and eventually transform low marsh regions into open water or  
60 mudflat areas (Alizad et al., 2018). SLR and navigational development can alter the tidal regime  
61 and long-wave propagation characteristics inside estuaries/bays and so change the flooding  
62 inundation patterns (Famikhilili et al., 2020; Khojasteh et al., 2021a, b). Similarly, hurricane  
63 impacts can create interior ponds, trigger shoreline erosion, and denude marshes (Morton and  
64 Barras, 2011). People and assets located in low-lying coastal regions and river deltas are frequently  
65 exposed to compound flooding. Challenges for flood hazard assessment unique to these systems  
66 include compounding effects of multiple flooding mechanisms, complex drainage systems with  
67 relatively low slopes, and periodically saturated soils. it is expected that between 0.2-4.6% of the



68 global population may be exposed to coastal flooding if no strategic adaptation takes place (Kulp  
69 and Strauss, 2019).

70 Efficient flood risk reduction strategies require accurate real-time assessment of flooding hazards  
71 (Gutenson, 2020; USGS Surface Water Information, 2021). In order to simulate the coastal flood  
72 hazard in wetlands, two-dimensional (2D) hydrodynamic models are commonly used for flood  
73 inundation mapping, as they allow for simulating complex oceanic, hydrological, meteorological,  
74 and anthropogenic processes based on process-based numerical schemes. The advanced circulation  
75 model (ADCIRC) (Luettich et al., 1992), DELFT3D (Roelvink and Banning, 1995), and  
76 LISFLOOD-FP (Bates et al., 2010) are among the most commonly used 2D hydrodynamic models  
77 for coastal flood hazard assessment in low-lying areas at local and regional scales (Bates et al.,  
78 2021; Muis et al., 2019; Thomas et al., 2019). Nonetheless, hydrodynamic modeling approaches  
79 require huge computational resources to conduct flood hazard assessments at a large scale. This is  
80 even more challenging when emergency responders need timely flood risk information at a  
81 desirable accuracy and resolution on a real-time basis. Therefore, while 2D hydrodynamic models  
82 are still a key component in many frameworks for detailed analyses of the flood hazard, the use of  
83 low-complexity flood mapping (LCFM) methods is essential for the preliminary estimation of  
84 areas exposed to flooding in a short time. Applying LCFM methods together with detailed  
85 hydrodynamic models provide a more comprehensive set of information for emergency responders  
86 and improve the efficiency of flood risk management in practice.

87 The advent of Digital Elevation Models (DEMs) has led to the development of a series of GIS-  
88 based LCFM methods for rapid estimation of flood hazard in the last couple of decades (Afshari  
89 et al., 2018; Dodov and Fofoula-Georgiou, 2006; Manfreda et al., 2011; McGlynn and  
90 McDonnell, 2003; McGlynn and Seibert, 2003; Nardi et al., 2006; Samela et al., 2016; Teng et al.,



91 2015; Williams et al., 2000). Among these methods, binary classification of a hydrogeomorphic  
92 raster has been shown to be an efficient approach for reliable delineation of floodplains (Degiorgis  
93 et al., 2012; Manfreda et al., 2014). In a binary hydrogeomorphic classification approach, the study  
94 area is examined as a grid of cells, then a threshold of a hydrogeomorphic feature, typically  
95 calculated from a DEM, is chosen. Comparing the hydrogeomorphic feature value of cells with  
96 the threshold, the entire study area is classified into flooded and non-flooded cells.

97 The Federal Emergency Management Agency (FEMA) provides flood hazard maps across the  
98 United States. These maps, also referred to as Flood Insurance Rate Maps (FIRMs) identify flood-  
99 prone areas corresponding to specific return periods. While these hazard maps provide useful  
100 information for a few recurrence intervals, they are no longer reliable for extreme flood events  
101 characterized by lower frequencies or longer return periods. In 2015, the National Water Center  
102 Innovators Program initiated the national flood interoperability experiment (NFIE) for real-time  
103 flood inundation mapping across the United States (Maidment, 2017; Maidment et al., 2014). The  
104 plan highlighted the tendency for event-based flood mapping which is more valuable and practical  
105 for emergency response and warning systems. Unlike past DEM-based methods that mostly  
106 focused on flood hazard mapping, Zheng et al., (2018b) proposed the development of DEM-based  
107 synthetic rating curves for real-time flood inundation mapping. In most current, real-time flood  
108 mapping methods, the forecasted river flows and/or water surface elevation are typically fed into  
109 flood inundation libraries to simulate the upcoming flood inundation areas (IWRSS, 2015, 2013;  
110 Maidment, 2017; Wing et al., 2019; Zheng et al., 2018a). The computationally intensive and time-  
111 consuming nature of detailed hydrodynamic models to numerically route flood waves typically  
112 restricts their usage in supporting emergency response activities (Gutenson et al., 2021;  
113 Longenecker et al., 2020).



114 An LCFM method based on Height Above Nearest Drainage (HAND) has been widely used and  
115 recognized as one of the best classifiers for identifying flood hazard areas (Degiorgis et al., 2012;  
116 Jafarzadegan et al., 2018; Jafarzadegan and Merwade, 2019; McGrath et al., 2018; Samela et al.,  
117 2017; Zheng et al., 2018a). The performance assessment of HAND classifiers in different  
118 topographic settings suggests, despite an acceptable performance in most locations, the accuracy  
119 of hazard maps is significantly lower in low-lying coastal regions (Jafarzadegan and Merwade,  
120 (2017) and Samela et al., (2017)). While the majority of DEM-based flood hazard mapping  
121 methods have been developed and tested for inland floods, access to an appropriate DEM-based  
122 method for coastal flooding is lacking in the literature. Since coastal flooding occurs rapidly and  
123 the time for hydrodynamic modeling and designing flood mitigation strategies is limited especially  
124 in data-scarce regions, efficient DEM-based approaches can be significantly beneficial for  
125 emergency and response-related decision-makers.

126 The overarching goal of this study is to propose a DEM-based LCFM method for coastal wetlands,  
127 estuaries, and deltas. To our knowledge, this is the first study that investigates the application of  
128 hydrogeomorphic binary classifiers for flooding in semi-flat coastal zones. We modify the HAND  
129 commonly used for riverine inland flooding (Degiorgis et al., 2013; Jafarzadegan et al., 2020;  
130 Samela et al., 2017) and propose a composite hydrogeomorphic index for tidally-influenced  
131 coastal regions. We enhance the applicability of the proposed method by developing  
132 hydrogeomorphic threshold operative curves for coastal flood hazard mapping. Unlike previous  
133 studies that rely on binary classifiers for specific return periods, the operative curves here offer a  
134 unique opportunity for rapid assessment of hazardous areas in real-time. These curves have  
135 substantial benefits for emergency responders when wetlands are prone to coastal flooding.



136 **2. Study area and data**

137 We study the Savannah River delta located in the Southeast United States, Georgia (Figure 1a).  
138 The morphology of this region is relatively complex due to the existence of a braided river  
139 followed by a dense drainage network of interior rivers and tidal creeks. This region is mostly  
140 characterized by its unique ecology including vast wetlands and saltmarsh ecosystems.

141 To simulate the flood hazard in this region, a mesh boundary encompassing the Savannah River  
142 delta, surrounding areas, and a portion of the Atlantic Ocean is generated (Figure 1b). Two U.S.  
143 Geological Survey (USGS) gauges, located at the Savannah River (#02198500, #02198690) and  
144 the Fort Pulaski station of the National Oceanic and Atmospheric Administration (NOAA) are  
145 used as upstream and downstream boundary conditions of the hydrodynamic model, respectively.  
146 Fort Pulaski station (NOAA – 8670870) counts with an 85-year length of records (since 1935) that  
147 enables a proper characterization of coastal flooding for design levels at lower frequencies or  
148 relatively large return periods. We select this region as a testbed because of 1) frequent coastal  
149 flooding induced by large semidiurnal tidal amplitudes at the estuary mouth (Cowardin et  
150 al., 2013) and 2) exposure of more than twenty thousand people settled in four developed areas,  
151 the Whitmarsh, Talahi, Wilmington, and Tybee Islands located in this region (Figure 1c).

152 The high-resolution DEM used as the base of our proposed hydrogeomorphic index is a 3 m light  
153 detection and ranging (LiDAR) that includes topographic and bathymetric (topobathy) data. This  
154 dataset has been developed by the NOAA's National Centers for Environmental Information  
155 (NCEI) and is available at the NOAA's Data Access Viewer repository  
156 (<https://coast.noaa.gov/dataviewer/>). The topobathy data was further corrected for wetland  
157 elevation error using the DEM-correction tool developed by Muñoz et al., (2019) in order to  
158 minimize vertical bias errors commonly found in LiDAR-derived coastal DEMs (Alizad et al.,



159 2018; Medeiros et al., 2015; Rogers et al., 2018). The vertical and horizontal accuracy of the DEM  
160 are 50 and 100 cm, respectively and its vertical datum is the North American Vertical Datum 1988  
161 (NAVD88). Land cover maps are obtained from the 2016 National Land Cover Database (NLCD)  
162 available at (<https://www.mrlc.gov/>). River discharge and WL records are obtained from the USGS  
163 (<https://maps.waterdata.usgs.gov/mapper/index.html>) and NOAA  
164 (<https://tidesandcurrents.noaa.gov/>), respectively. In addition, post-flood high water marks  
165 (HWMs) of Hurricane Irma and Matthew are obtained from the USGS Flood Event Viewer  
166 platform (<https://stn.wim.usgs.gov/FEV/>). These high-water marks are used for calibration and  
167 validation of the Savannah model in Delft3D-FM.

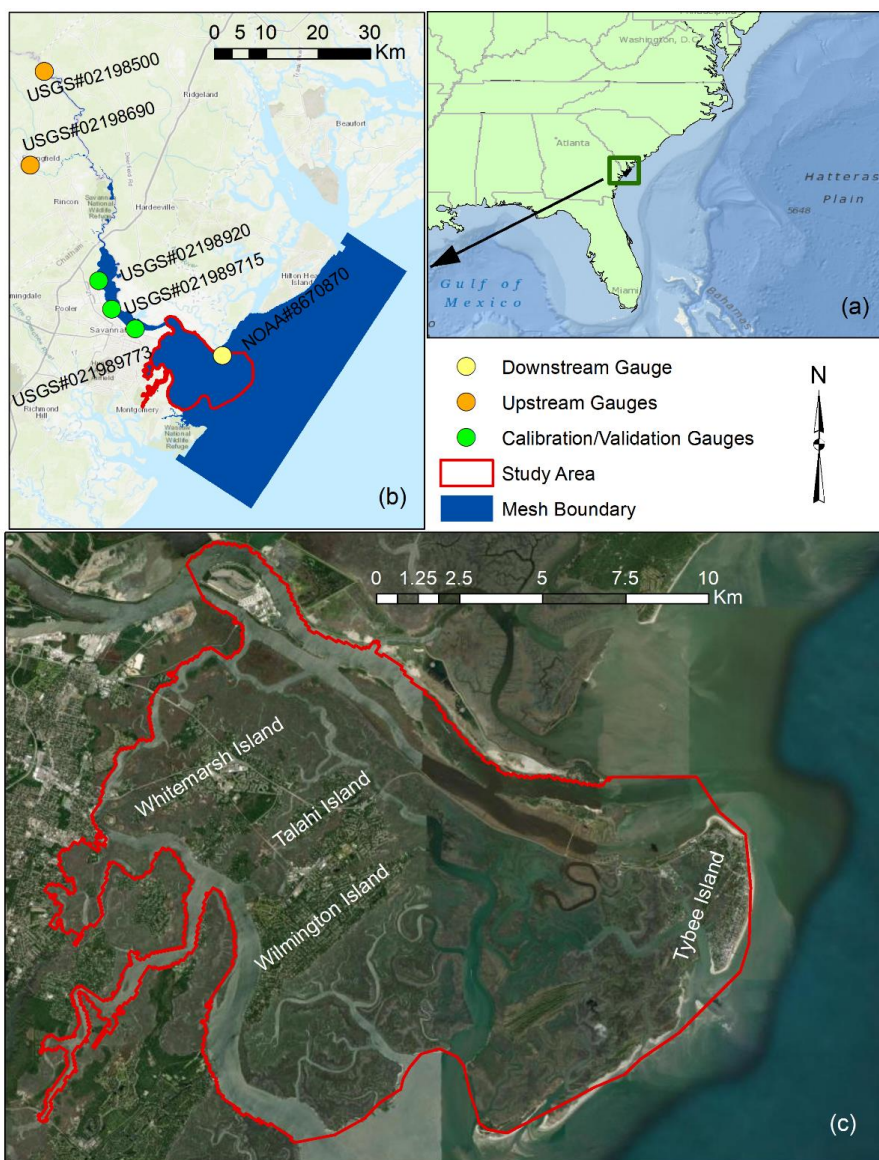
168

169





170



171

172 **Figure 1.** Map of the study area and mesh boundary of the hydrodynamic model. (a) the geographic  
173 location of the study area in the southeast U.S., (b) The mesh boundary used by the hydrodynamic  
174 model (blue) for flood inundation mapping as well as the location of upstream (orange),



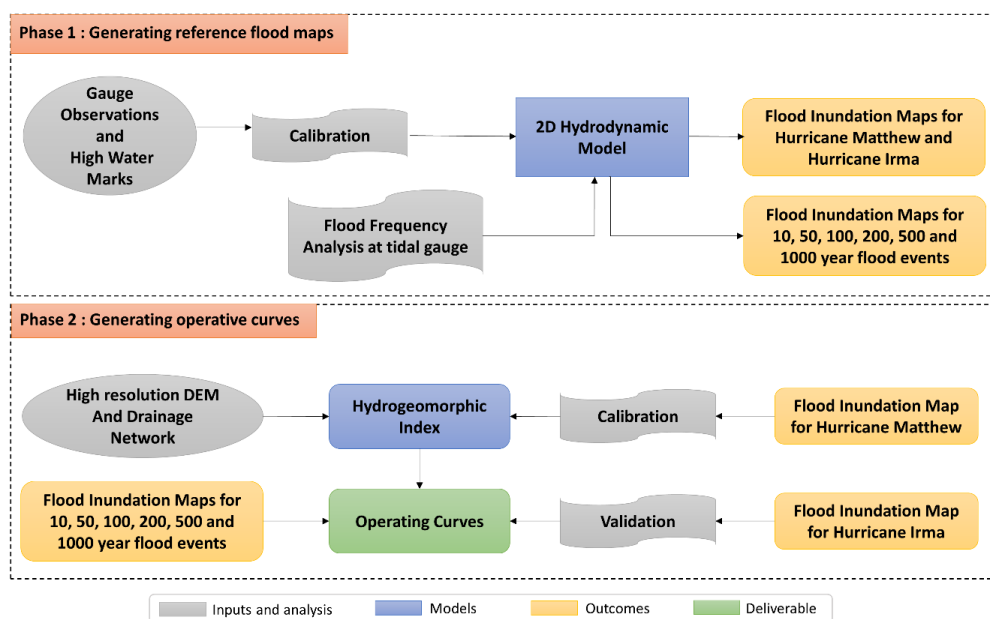
175 downstream (yellow), and calibration/validation (green) gauges, and (c) the boundary of Savannah  
176 wetlands used as the case study along with urbanized areas. (ESRI 2018)

### 177 **3. Methods**

178 We propose a DEM-based LCFM approach for the rapid assessment of flood hazard areas in real-  
179 time. The proposed approach consists of two phases (Figure 2). In phase 1, a 2D hydrodynamic  
180 model is calibrated based on observed WLs at USGS gauges and HWMs that are available during  
181 Hurricane Matthew in 2017. We then use the calibrated hydrodynamic model to generate a flood  
182 inundation map that serves as a reference map in the next phase. In addition, for flood frequency  
183 analysis, we perform block maxima sampling approach to select the annual WL maxima at Fort  
184 Pulaski station. The selected samples are then used to estimate return levels for six return periods  
185 of 10, 50, 100, 200, 500, and 1000 year floods. Using these estimated WLs as the main boundary  
186 conditions of the hydrodynamic model, we also generate six flood inundation maps corresponding  
187 to these return periods. In phase 2, we use a high-resolution DEM together with the drainage  
188 network data to calculate the hydrogeomorphic index. Subsequently, the flood inundation map  
189 generated for Hurricane Matthew in phase 1, is used as a reference map to calibrate the  
190 hydrogeomorphic index. Then, the calibrated index uses the flood inundation maps provided for  
191 different return periods in phase 1 to develop the operative curves. These curves form the basis for  
192 the rapid assessment of flood hazard areas for any upcoming coastal flood event in the future. To  
193 validate the effectiveness and reliability of the developed operative curves, we use them to identify  
194 hazard areas corresponding to Hurricane Irma, and then we compare their accuracy with the  
195 reference map provided by the hydrodynamic model for this flood event. In the following sections,  
196 we further explain the hydrodynamic model, flood frequency analysis, and hydrogeomorphic  
197 method, respectively.



198



199

200 **Figure 2.** Flowchart of the proposed approach for generating hydrogeomorphic threshold  
201 operative curves. In Phase 1, the 2D hydrodynamic model is calibrated and generates the required  
202 reference maps for the next phase. In Phase 2, the reference maps are used in conjunction with the  
203 hydrogeomorphic index to generate the operative curves for fast and real-time coastal flood hazard  
204 assessment.

### 205 3.1 Hydrodynamic Model

#### 206 3.1.1 Model setup

207 We use the 2019 Delft3D-FM suite package (Deltares, 2019) to model the complex riverine,  
208 estuarine, and intertidal flat hydrodynamics in the Savannah River delta and wetland regions. The  
209 suite package has been used in similar coastal studies characterized by vast wetland regions with  
210 satisfactory results (Fagherazzi et al., 2014; Kumbier et al., 2018; Sullivan et al., 2019). Moreover,  
211 the model developed for Savannah has been used in other studies to simulate extreme and non-  
212 extreme events including Hurricane Matthew that hit the southeast Atlantic Coast in October 2016



213 (Muñoz et al., 2021, 2020). The 2D hydrodynamic model comprises nearly 85 km of the Savannah  
214 River extending from Fort Pulaski station (NOAA – 8670870) at the coast up to Clyo station  
215 (USGS – 02198500). The model consists of an unstructured triangular mesh to ensure a correct  
216 representation of geomorphological settings including sinuous and braided river waterways and  
217 relatively narrow tidal inlets. Furthermore, the mesh has a spatially varying cell size ranging from  
218 1.5 m in the upstream riverine area, 10 m over wetland regions, 120 m along the coast, and up to  
219 1.4 km over the Atlantic Ocean (Figure 1b).

### 220 **3.1.2 Model calibration**

221 For calibration purposes, the model was forced with time series of river flow obtained from Clyo  
222 station as an upstream boundary condition (BC), coastal WL from Fort Pulaski station as a  
223 downstream BC, and with spatially varying Manning's roughness values ( $n$ ) classified into open  
224 water, wetland, urban, and riverine areas. The optimal (or calibrated) set of  $n$ -values were inferred  
225 from 200 model simulations of Hurricane Matthew, as this event reported the highest peak WL at  
226 Fort Pulaski station since the year 1935 (2.59 m w.r.t. NAVD88). Each simulation was conducted  
227 in a high-performance computing system and included a one-month warm-up period and a unique  
228 set of  $n$ -values generated with the Latin Hypercube Sampling (LHS) technique (Helton and Davis,  
229 2003). The range of  $n$ -values was derived from pertinent literature and included hydrodynamic  
230 modeling and open channel flow studies (Arcement and Schneider, 1989; Chow Ven, 1959; Liu et  
231 al., 2019). The set of values achieving both the lowest Root Mean Square Error (RMSE) and  
232 highest correlation coefficient ( $R^2$ ) around the peak WL (e.g., 7-day window) was selected as the  
233 optimal one and further used for coastal flood simulations. The calibrated  $n$ -values used in this  
234 Savannah model are: open water ( $n = 0.027$ ), wetland ( $n = 0.221$ ), urban ( $n = 0.03$ ), and  
235 downstream/upstream riverine areas ( $n = 0.037$  and  $n = 0.086$ , respectively)



### 236 3.2 Flood Frequency Analysis

237 Preliminary model simulations indicate a negligible influence of river flow on coastal wetland  
238 inundation as compared to storm surge at Wassaw Sound, Wilmington, and Tybee islands (Figure  
239 1c). This can be explained by the proximity of the islands to the Atlantic Ocean as well as  
240 freshwater runoff regulation and flood controls by three large dams located upstream of the Clyo  
241 station (USGS – 02198500), namely J. Strom Thurmond, Richard B. Russell, and Hartwell  
242 (Zurqani et al., 2018). We, therefore, conduct a univariate flood frequency analysis based on  
243 annual block maxima sampling of WLs observed at the Fort Pulaski station (NOAA – 8670870).  
244 We use the ‘*allfitdist*’ tool in MATLAB to find the best parametric probability distribution fit to  
245 the data, based on Maximum Likelihood, Bayesian information criterion (BIC), or Akaike  
246 information criterion (AIC).

### 247 3.3 Hydrogeomorphic index

248 Among different hydrogeomorphic features used for flood hazard mapping, HAND (sometimes  
249 also referred to as feature  $H$ ) has been widely used as one of the best indicators of floodplains.  
250 However, due to the weakness of this feature for proper characterization of floodplains in flat  
251 regions and coastal areas, here we develop a composite hydrogeomorphic index that considers  $H$   
252 as well as the distance to the nearest drainage ( $D$ ). Although the overall performance of feature  $D$   
253 is less than  $H$  in most case studies (Degiorgis et al., 2012; Manfreda et al., 2015a; Samela et al.,  
254 2016), feature  $D$  can be a better descriptor of floodplains in highly flat regions according to the  
255 study conducted by Samela et al., (2017). In another study, Gharari et al., (2011) proposed a  
256 composite index by multiplying both features  $H$  and  $D$  and demonstrated that  $H$  is a better feature  
257 compared to the case that both features are used for landscape classification. The main drawback  
258 of their proposed index was that they used the same weights for both features which result in



259 degrading the classification performance. To overcome the limitation of the proposed index and  
260 to consider the key role of feature  $D$  in flat areas, we maintain feature  $D$  in our composite index  
261 and add different weights to  $H$  and  $D$  using Eq. 1 as follows:

$$262 \quad I_{HD} = \left(\frac{H}{H_{max}}\right)^{w1} \times \left(\frac{D}{D_{max}}\right)^{w2} \quad \text{where} \quad w1 + w2 = 1 \quad (1)$$

263 In Eq.1,  $H_{max}$  and  $D_{max}$  denote the maximum value of raster  $H$  and  $D$  used for normalizing the  
264 hydrogeomorphic index whereas  $w1$  and  $w2$  refer to the weights of feature  $H$  and  $D$ , respectively.  
265 The conditional equation of  $w1 + w2 = 1$  helps lower the computational burden of the calibration  
266 procedure by reducing the number of unknown parameters from two to one. Figure 3 illustrates an  
267 example of calculating the  $I_{HD}$  index with a given set of weights ( $w1=0.6$  and  $w2=0.4$ ) for the  
268 study area. Using a high-resolution coastal DEM (Figure 3a), raster  $H$  and  $D$  are calculated  
269 (Figures 3b and 3c). Considering a DEM with  $N$  cells, the main step is to find a coordinate matrix  
270 that indicates the location of the nearest stream cell to each grid cell. Knowing this matrix and the  
271 number of cells required to cross the nearest stream cell, the feature  $D$  is calculated. The coordinate  
272 matrix can also be used in conjunction with the DEM to calculate the feature  $H$ . In order to  
273 calculate the hydrogeomorphic index  $I_{HD}$ , the weights in Eq. 1 are calibrated using a reference  
274 flood hazard map obtained from hydrodynamic simulation (e.g., Hurricane Matthew). We test  
275 different combinations of weight parameters ( $w1$  and  $w2$ ) to find the importance of features  $H$   
276 and  $D$ , and then finalize the hydrogeomorphic index with known parameters for future flood hazard  
277 mapping. We further validate the weight parameters with simulations of Hurricane Irma.

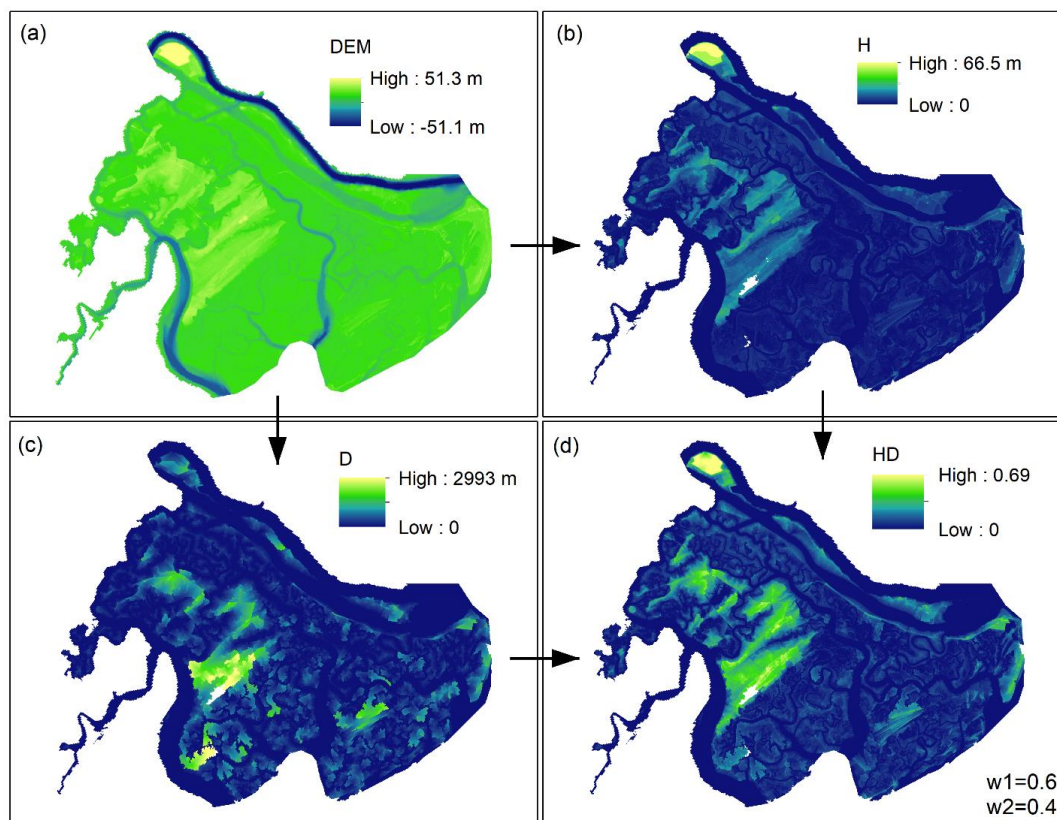
278

279





280



281

282 **Figure 3.** The required steps for calculating the proposed hydrogeomorphic index. A high-  
283 resolution coastal DEM (3 m) is used as the source data to (a) generate the Height Above nearest  
284 Drainage ( $H$ ) and the Distance to the nearest Drainage ( $D$ ), respectively (b, c). Using Eq. 1, the  
285 normalized features  $H$  and  $D$  are multiplied with different weights to generate the  
286 hydrogeomorphic index (d).

### 287 3.4 Binary classifiers for flood hazard mapping

288 Considering the study area as a grid of cells, a binary classifier assigns a value of zero or one to  
289 each cell and generates a map of two different classes. In flood hazard mapping, the common



290 approach is to define a threshold on a hydrogeomorphic index (e.g.  $I_{HD}$ ) and use the following if-  
291 and-else rule for the classification:

$$292 \quad f(i) = \begin{cases} 1 & I_{HD}^i \leq TH \\ 0 & I_{HD}^i > TH \end{cases} \quad (2)$$

293 where  $f(i)$  and  $I_{HD}^i$  denote the label of flood hazard map and the proposed hydrogeomorphic  
294 index value at cell  $i$ , respectively, and  $TH$  denotes the threshold of the hydrogeomorphic classifier  
295 that should be calibrated. The flood hazard map generated with the binary classifier is compared  
296 with a binary reference hazard map, and the rate of true positive ( $rtp$ ), rate of false positive ( $rfp$ ),  
297 and *error* are calculated as follows (Jafarzadegan and Merwade, 2017):

$$298 \quad rtp = \frac{\text{True positive instances}}{\text{Total positives}} \quad (3)$$

$$299 \quad rfp = \frac{\text{False positive instances}}{\text{Total negatives}} \quad (4)$$

$$300 \quad \text{error} = rfp + (1 - rtp) \quad (5)$$

301 In binary classification, positive and negative refer to a value of one and zero, respectively. True  
302 positive instances are those positive cells that are correctly predicted by the classifier and false  
303 positive instances represent those negative cells that are wrongly classified as positive. The *error*,  
304 reflecting all cells that are wrongly predicted by the classifier, is a commonly-used measure for  
305 validating the performance of binary classifiers for flood hazard mapping. Another useful  
306 performance measure to validate the binary classifier is the area under the curve (AUC) of the  
307 Receiver Operating Characteristic (ROC) graph proposed by Fawcett, (2006).

308 To calibrate the binary classifier we minimize the *error* while searching for the optimum  $TH$  value.  
309 In this optimization problem, the reference flood hazard map used for calculating the *error* is the





310 key input that should be further described. The flood inundation maps generated by the  
311 hydrodynamic model indicate WLs at different cells in different time steps and should be  
312 converted to a single binary map. A common approach used for inland floods is to find the  
313 maximum inundation area over the entire flooding period and then assign all cells with zero WL  
314 to “dry” or “non-flooded” and other cells with positive values as “wet” or “flooded”. In delta  
315 estuaries and coastal regions nearby the ocean, however, almost all cells can be flooded with small  
316 WL values. Therefore, after finding the maximum inundation over the flooding period, we use  
317 another set of binary labels as “low hazard” vs “high hazard” and define the hazard depth cutoff  
318 (HDC) as a threshold used to convert a continuous map of WL to a binary map with only two  
319 labels. Depending on the HDC used for distinguishing low from high hazard regions, the reference  
320 flood map is changed which results in a different calibrated  $TH$ . In addition to HDC, the intensity  
321 of the flood event shown with the return period ( $T$ ) also changes the reference flood hazard map.  
322 Therefore, the calibrated parameter  $TH$  is a function of both HDC and  $T$  and the main goal of this  
323 study is to provide operative curves showing the variation of  $TH$  with these two factors. We run  
324 the hydrodynamic model for 6 different return periods of 10, 50, 100, 200, 500, and 1000 year  
325 events and then convert the WL maps to binary maps using 21 HDC resulting from 0.1 increments  
326 in the range of 0-2 m. The binary classification and calibration of  $TH$  are performed for different  
327 reference maps generated from various combinations of  $T$  and HDC.

#### 328 **4. Results**

329 A comprehensive calibration and validation of the Savannah River model is shown in Figure 4.  
330 This step is crucial to ensure that the flood hazard maps provided by the model are reliable enough  
331 to be used as the reference of the hydrogeomorphic method. We assess the performance of the  
332 model by first comparing simulated and observed WLs at four USGS stations along the Savannah

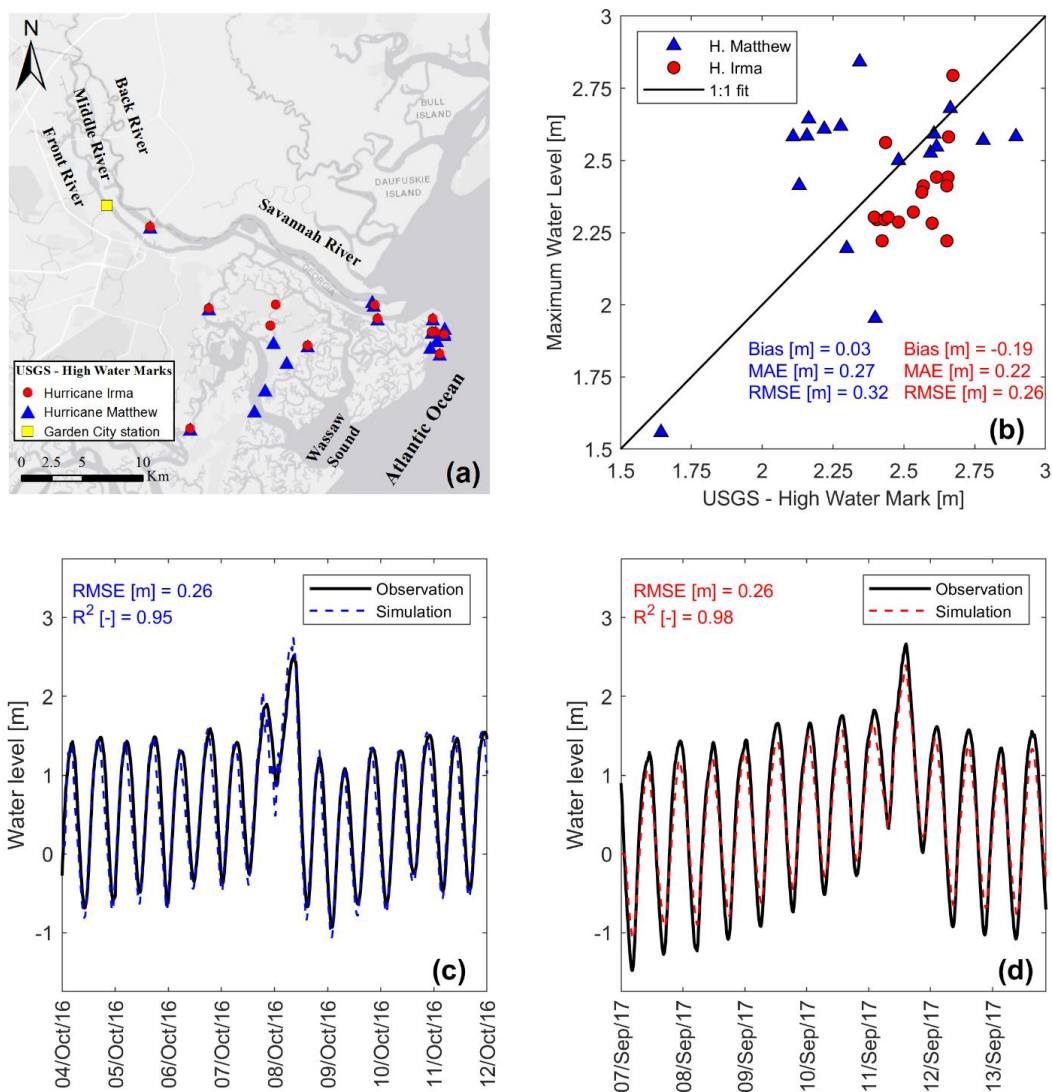


333 River (Figure 1b, green circles). For convenience, we only present simulated and observed WLs  
334 of Hurricane Matthew and Irma at Garden City (Figure 4c and 4d, respectively) located at ~29.5  
335 km from the river mouth (Figure 4a, yellow square). The results of the remaining stations are  
336 included in the supplementary material (Figure S1). The RMSE and  $R^2$  of the gauges stations  
337 remain below 30 cm and above 0.90, respectively, for the two hurricane events, which is reflective  
338 of satisfactory model performance. Overall, the magnitude and timing of the highest peak WL  
339 observed during the hurricanes are well captured by the Savannah River model. To further evaluate  
340 the model performance in coastal flood propagation analysis, we compare maximum WLs  
341 resulting from model simulations with the USGS HWMs collected in urban and surrounding  
342 wetland areas (Figure 4b). The 1:1 line represents a perfect fit between simulated and observed  
343 maximum WLs and helps visualize overestimation (above the 1:1 line) and underestimation of the  
344 model. Similarly, the evaluation metrics indicate a satisfactory performance of the model with a  
345 slightly over- and underestimation during Matthew and Irma. Moreover, the model achieves a  
346 relatively small RMSE ( $< 35$  cm) and MAE ( $< 30$  cm).

347



348

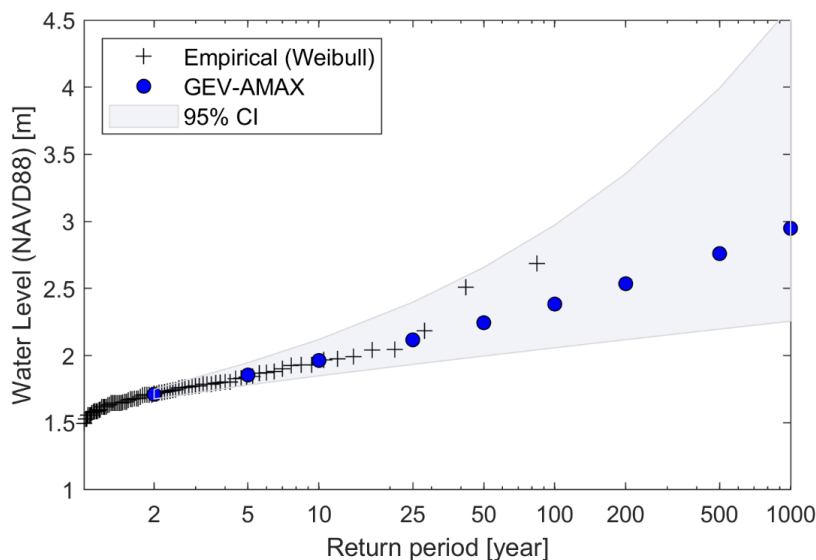


349

350 **Figure 4.** Calibration and validation of the Savannah Delft3D-FM model. (a) Location of high-  
351 water marks (HWMs) in the Savannah River delta for Hurricane Mathew (blue triangles) and  
352 Hurricane Irma (red circles). (b) Comparison between simulated maximum WLs and HWMs in  
353 Savannah. (c and d) Time series of simulated and observed WLs at Garden station for Hurricane  
354 Mathew and Hurricane Irma, respectively.



355 To generate boundary conditions for coastal flood modeling simulations associated with the  
356 proposed return periods, we perform flood frequency analysis of coastal WL at the Fort Pulaski  
357 station (in Figure 5) located at the mouth of the Savannah River (Figure 1b, yellow circle). In this  
358 study, we select Generalized Extreme Value (GEV) because of its smallest estimated BIC  
359 compared to other parametric distributions available at the *'allfitdist'* tool. In addition, we show  
360 the 95% confidence bounds of the GEV distribution and fit a non-parametric Weibull distribution  
361 to the data for comparison purposes. Hereinafter, we will use the GEV distribution to estimate  
362 WLs for 10, 50, 100, 200, 500, and 1000-year return periods.



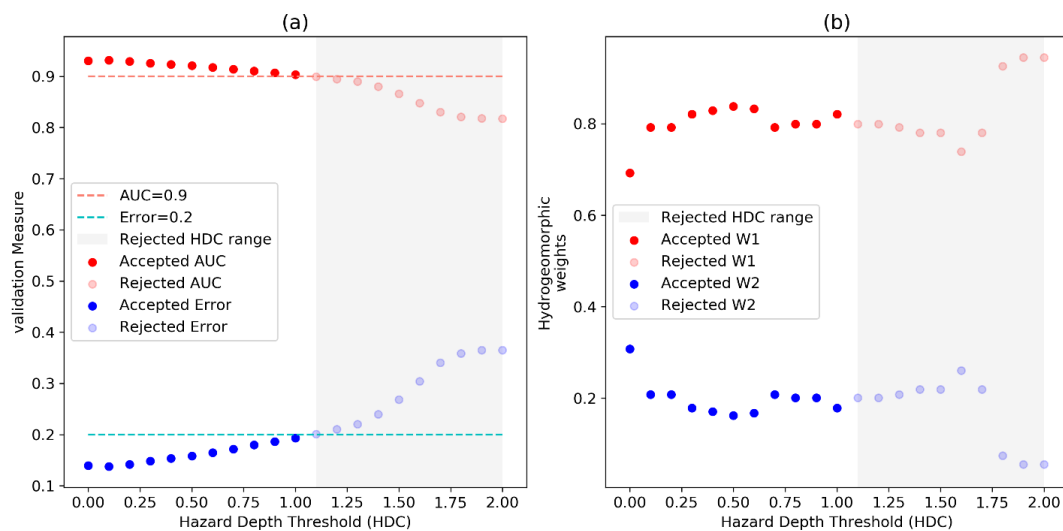
363

364 **Figure 5.** Return WLs for Fort Pulaski station in Savannah GA (NOAA - 8670870). Plotting  
365 positions (black crosses) are derived from the Weibull formula based on annual block maxima  
366 time series (AMAX) and comparable to the Generalized Extreme Value (GEV) distribution (blue  
367 circles). 95% confidence intervals (CI) for the distribution parameters of the GEV distribution are  
368 shown with a shaded blue band.

369



370 After calibrating the Delft3D-FM model, we generate daily flood inundation maps for Hurricane  
371 Matthew, determine the maximum flood extent among all days, and then use an HDC to convert  
372 the maximum inundation map to a binary map of low and high hazard classes. Using 21 different  
373 HDCs ranging from 0 to 2 m, we perform 21 calibrations corresponding to a given reference flood  
374 hazard map generated from a specific HDC value. Figure 6a shows the *error* and AUC of  
375 calibration corresponding to different HDC values. As can be seen, increasing the HDC decreases  
376 the accuracy of the hydrogeomorphic method for flood hazard mapping. Looking into the errors  
377 and AUC values reported in the literature of binary flood hazard mapping studies, we consider an  
378 error of 0.2 and an AUC of 0.9 (dash lines) as the limits for distinguishing acceptable models from  
379 unacceptable ones. The grey region indicates the rejected HDC values above 1.1 m that result in  
380 unacceptable accuracy (e.g.,  $\text{Error} > 0.2$  or  $\text{AUC} < 0.9$ ). Figure 6b indicates the optimum weights  
381 calculated from the calibration of the hydrogeomorphic method corresponding to different HDC  
382 values. The higher value of  $w_1$  compared to  $w_2$  demonstrates that feature  $H$  is a more important  
383 factor than feature  $D$  in representing the flood hazard areas, and a combination of both features is  
384 the best indicator of floodplains compared to using each feature individually ( $w_1 = 0$  or  $w_2 = 0$ ).  
385 Figure 6b also shows that for the  $\text{HDC} = 0$  (wet vs dry classification), feature  $D$  shows the highest  
386 contribution (30%) while using the high HDC value of 2 m decreases the contribution of this  
387 feature to almost zero.



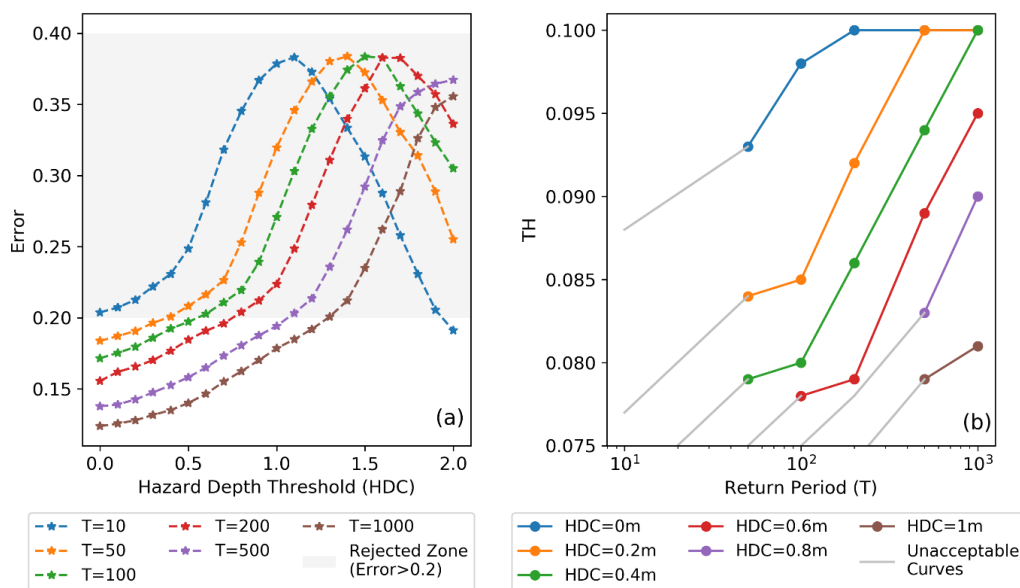
388

389 **Figure 6.** Calibration of Hydrogeomorphic index for Hurricane Matthew. (a) the variation of  
390 performance measures AUC (red) and error (blue) for different HDC values and (b) the optimum  
391 weights of the hydrogeomorphic index for different HDC values. The dash lines show the  
392 maximum error (0.2) and minimum AUC (0.9) that are acceptable for flood hazard mapping. Using  
393 these criteria, the gray regions show that the hydrogeomorphic model cannot provide acceptable  
394 results for HDC values higher than 1.1 m.

395 To generate the operative curves for future flood events, we design 36 scenarios that include 6  
396 HDCs (0, 0.2, 0.4, 0.6, 0.8, 1 m) from the acceptable range of 0-1 m for six different reference  
397 hazard maps, provided by the Delft3D-FM model for return periods of 10, 50, 100, 200, 500, and  
398 1000 years. Each scenario provides a reference hazard map, so a binary classification is performed  
399 to estimate TH corresponding to each scenario. Figure 7a indicates the error curves for different  
400 return period events. For low HDCs, increasing the magnitude of the flood (higher return period)  
401 results in more accuracy of the hydrogeomorphic method. This pattern is opposite for high HDCs  
402 where flood event with a 10 year return period provides the highest accuracy. In general, the grey



403 region shows that for high HDCs, the performance of the hydrogeomorphic method is poor for  
 404 almost all return periods while for low HDCs, all flood events can be accurately used for flood  
 405 hazard mapping. Figure 7b illustrates the hydrogeomorphic threshold operative curves for future  
 406 flood hazard mapping. The  $TH$  in the y-axis is the key value that can be estimated for each  
 407 combination of HDC and return period. Knowing this threshold, Eq. 2 can be used to rapidly  
 408 estimate the hazard areas for future floods. As expected, a higher magnitude of flood needs a higher  
 409 hydrogeomorphic threshold while increasing HDC (smaller high-hazard areas) requires a smaller  
 410 threshold for binary classification. The grey parts of the curves refer to those scenarios that have  
 411 unacceptable accuracy so it is recommended to not use HDCs corresponding to these parts.



412

413 **Figure 7.** (a) The errors of flood hazard maps generated by the calibrated hydrogeomorphic  
 414 method for different return period flood events and HDC values. (b) The hydrogeomorphic  
 415 threshold operative curves provided for different HDC values. These operative curves are the



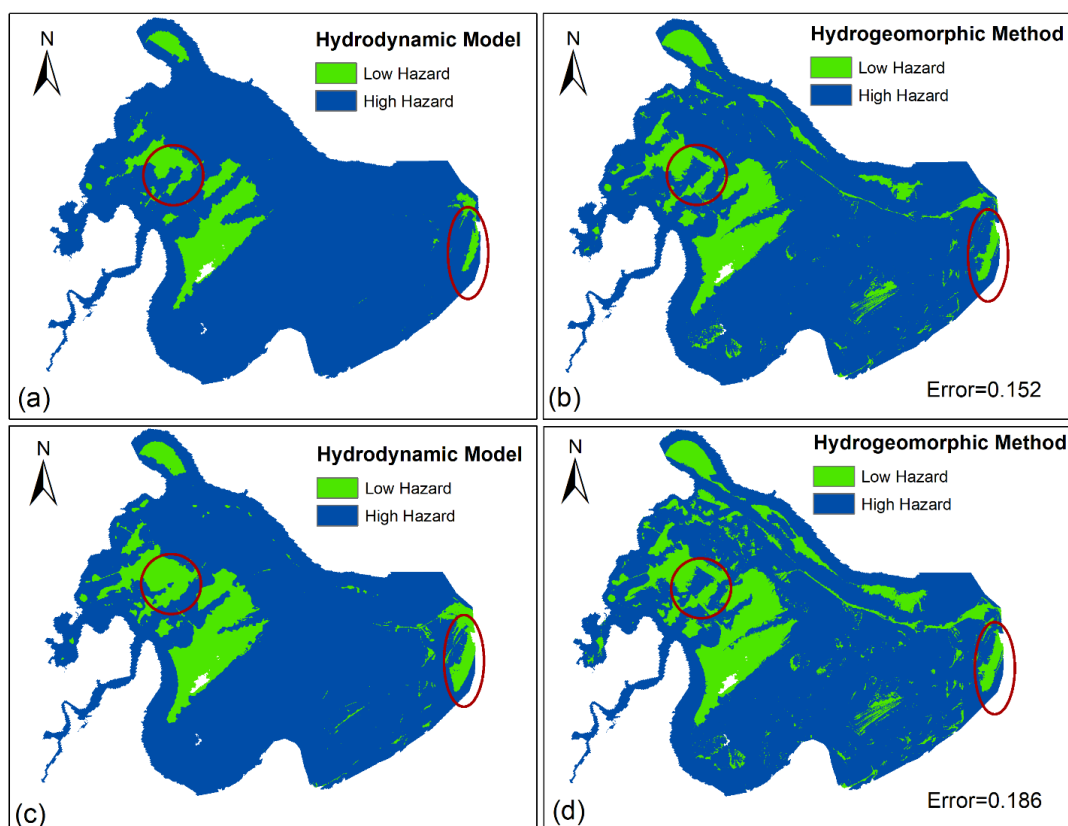
416 major tool for fast flood hazard mapping as depending on the return period of a future flood event  
417 and the HDC value chosen by the decision-maker, the operative curves estimate the  
418 hydrogeomorphic threshold. Knowing this threshold, the flood hazard map will be generated in a  
419 few minutes.

420 Finally, we evaluate the accuracy and effectiveness of the proposed operative curves by validating  
421 their performance in generating flood hazard areas during Hurricane Irma. The maximum WL  
422 during this flood event was 2.49 m that corresponds to a 223-year flood event according to our  
423 flood frequency analysis (e.g., GEV distribution). For two HDCs of 0 and 0.6 m, the operative  
424 curves suggest the hydrogeomorphic thresholds of 0.1 and 0.08, respectively. Using these  
425 thresholds and Eq.2, the flood hazard maps corresponding to Hurricane Irma can be generated.  
426 Figure 8 indicates a side by side comparison of flood hazard maps generated by the Delft3D-FM  
427 model (Figures 8a and 8c) and the hydrogeomorphic threshold operative curves (Figures 8b and  
428 8d) for two different HDCs of 0 (Figures 8a and 8b) and 0.6 m (Figures 8c and 8d). For both HDCs,  
429 errors (0.152 and 0.186) are less than a 0.2 limit used for reliable flood hazard mapping. The main  
430 errors of the hydrogeomorphic method are some noisy scattered low-hazard areas located in the  
431 east and southeast of the study area. The red circle in the left part of the figures also shows a region  
432 that the hydrogeomorphic method cannot properly simulate, especially for higher HDCs. On the  
433 other hand, the red eclipse at the right side of the figures illustrates an urbanized region where the  
434 hydrogeomorphic method properly classifies the area compared to the reference map. Overall, the  
435 high overlap of the flood hazard maps provided by the hydrogeomorphic method with the reference  
436 maps provided by the hydrodynamic model (error <0.2) illustrates the reliability and effectiveness  
437 of the proposed hydrogeomorphic method for flood hazard mapping. Besides, the high efficiency  
438 of this approach for rapid estimation of flood hazard maps (order of minutes) compared to the long





439 computational time required for detailed hydrodynamic modeling (order of hours) suggests the  
440 proposed hydrogeomorphic method as an alternative for efficient flood hazard mapping during  
441 emergencies.



442

443 **Figure 8.** Validation results for Hurricane Irma showing a side-by-side comparison of flood  
444 hazard maps generated by the hydrodynamic model and hydrogeomorphic method for HDC=0  
445 (a, b) and HDC=0.6 m (c, d). To generate the flood hazard maps by the hydrogeomorphic  
446 method, the operative curves estimate two hydrogeomorphic thresholds of 0.1 and 0.08 for  
447 HDC= 0 m and HDC= 0.6 m, respectively while the return period of Hurricane Irma is estimated  
448 as a 223 years flood event.



## 449 **5. Discussion**

450 This study develops hydrogeomorphic threshold operative curves for rapid estimation of hazardous  
451 areas during emergencies of future coastal floods in deltas and estuaries. The low errors (<0.2) of  
452 estimated hazard maps for Hurricane Irma generated by the proposed approach compared to the  
453 reference hydrodynamic model results demonstrate the high accuracy of the proposed operative  
454 curves for future flood events in this region. According to studies conducted on the binary  
455 classification of hydrogeomorphic features in the literature, the errors of the best classifiers were  
456 mostly in the range of 0.2-0.3 for inland floods (Degiorgis et al., 2012; Manfreda et al., 2014).  
457 Therefore, given the more complexity of terrain and drainage network in deltas, predicting the  
458 hazard maps with errors less than 0.2 (e.g. error of 0.152 for HDC=0) is a promising achievement.  
459 The potential reasons explaining a high accuracy of the proposed binary classifier for wetlands  
460 include the high-resolution DEM used for mapping (~3m), and the incorporation of bathymetry  
461 into DEM. In addition, the flexible structure of the proposed hydrogeomorphic index, with two  
462 varying weights of *H* and *D* features, allows for calibrating the index with the optimum  
463 contribution of each feature, which in return results in the highest accuracy.

464 Unlike past studies that used binary classifiers for detecting hazard areas corresponding to past  
465 floods or generated static maps for a specific return period event (Degiorgis et al., 2012;  
466 Jafarzadegan et al., 2018; Manfreda et al., 2015b; Samela et al., 2017), here we propose the  
467 hydrogeomorphic threshold operative curves for real-time flood hazard mapping. Considering the  
468 rapid occurrence of hurricane-induced flooding in deltas and estuaries, these curves can be highly  
469 beneficial for emergency responders to provide a preliminary estimation of hazard areas for an  
470 upcoming flood in these regions and design the appropriate evacuation strategies. In addition, the  
471 proposed operative curves demonstrate the hydrogeomorphic threshold variations with HDCs.



472 This feature of the operative curves gives additional flexibility to decision-makers for estimating  
473 the hazard maps based on the HDC that is considered given the momentary safety issues. For  
474 example, identifying the hazard map based on  $HDC < 0.3$  is useful for checking the operability and  
475 accessibility of essential facilities and infrastructure, while a hazard map corresponding to  $HDC = 1$   
476 indicates those areas that experience high WLs above 1 m as hazardous areas, with greater potential  
477 for casualties and significant structural damage. Overall, the hydrogeomorphic threshold operative  
478 curves are a function of both the return period (flood severity) and HDC (a decision-making option  
479 that controls the definition of high hazard). Using a similar approach, future studies can provide  
480 these curves for inland floods as well. In addition, due to the practical benefits of these curves for  
481 efficient coastal flood hazard assessment, the hydrogeomorphic threshold operative curves can be  
482 extended to other deltas and estuaries that experience frequent flooding across the US (e.g.,  
483 Mississippi - LA, Galveston Bay - TX, Delaware Bay - DE, Chesapeake Bay - VA, among others)  
484 and the world (e.g. Yangtze - China, Brahmaputra - Bangladesh, among others).

485 The reference maps used for training the binary classifier are key components for generating  
486 reliable results. Since these reference maps are the outcomes of hydrodynamic modeling, they are  
487 prone to uncertainties stemming from unrealistic parametrization, imperfect model structure, and  
488 erroneous forcing. The design floods used as boundary conditions of the hydrodynamic model are  
489 estimated from flood frequency analysis that is prone to uncertainty as well. With access to less  
490 than 100 years of data for flood frequency analysis, the extreme return levels (i.e. 500 and 1000  
491 year floods) pose high uncertainties due to the extrapolation of annual maxima data. This should  
492 warn decision-makers to be more cautious about using operative curves for extreme flood events.  
493 For future studies, the uncertainty bounds of flood frequency analysis (especially extrapolations  
494 for extreme cases) can be considered in the modeling. In a real-time scenario, the forecasted WL



495 used for flood frequency analysis is also prone to uncertainties originating from imperfect  
496 forecasting methods and nonstationary climate data. In addition, the uncertainty of model  
497 parametrization can be accounted for by running the hydrodynamic model for different  
498 combinations of optimum parameters. Model structure uncertainty can be also considered by using  
499 different hydrodynamic models and combining the results. Finally, probabilistic reference maps  
500 together with uncertainties involved in WL forecasting and flood frequency analysis can be  
501 integrated to develop probabilistic hydrogeomorphic threshold operative curves in future studies.  
502 This is in line with the report provided for the NOAA National Weather Service (NWS), showing  
503 the NWS stakeholder's preference for utilizing probabilistic storm surge inundation maps in the  
504 future (Eastern Research Group, Inc, 2013). The probabilistic operative curves account for the  
505 major source of uncertainties and provide a more reliable decision-making tool for coastal flood  
506 hazard mapping.

507 The operative hydrogeomorphic threshold classifiers proposed for real-time coastal flood hazard  
508 mapping can be used as an alternative tool for the rapid estimation of hazardous areas. In the  
509 operational mode, the water level forecasts provided by the NWS can be used to estimate the return  
510 period of an upcoming coastal flood event. Using the proposed operative curves, the  
511 hydrogeomorphic threshold is determined and the flood hazard map is generated. The Sea, Lake,  
512 and Overland Surges from Hurricanes (SLOSH) model is an LCFM tool currently used by NWS  
513 to estimate probabilistic storm surge forecasts. The flood inundation maps generated by this model  
514 are the results of overlaying storm surge forecast with DEM. The model doesn't consider the  
515 streamflow network and riverine flood mechanisms. On the other hand, our proposed  
516 hydrogeomorphic index uses both streamflow network and DEM to provide a more detailed  
517 representation of the flooding in coastal areas. Another LCFM approach is to train machine



518 learning algorithms on reference inundation maps provided by well-calibrated hydrodynamic  
519 models (Bass and Bedient, 2018). A benchmark study that compares the performance (accuracy  
520 and efficiency) of three LCFM methods, including our proposed DEM-based hydrogeomorphic  
521 classifier, the surrogate machine learning-based algorithm, and the SLOSH model is highly  
522 recommended for future studies.

## 523 **6. Summary and Conclusion**

524 In this study, we proposed binary classifiers for efficient flood hazard mapping in deltas and  
525 estuaries. The HAND, typically used for inland flooding, is modified for flat regions along the  
526 coastline, and a new hydrogeomorphic index  $I_{HD}$  that comprises both HAND and distance to  
527 nearest drainage was developed. The DEM used as the base of these binary classifiers is a 3 m  
528 Lidar that includes bathymetric information. This is another improvement compared to previous  
529 DEM-based classifiers that commonly used 10-30 m DEMs without bathymetric data. The  $I_{HD}$   
530 index has two unknown weights that show the contribution of both HAND and feature  $D$ . We  
531 simulated Hurricane Matthew with the Delft3D-FM model and used the results as a reference flood  
532 hazard map to calibrate the  $I_{HD}$  index. Using Delft3D-FM again, we generated six flood hazard  
533 maps corresponding to different return periods and employed these maps as a reference to generate  
534 the hydrogeomorphic threshold operative curves. Finally, we validated the proposed operative  
535 curves for reliable and efficient flood hazard mapping by comparing the flood hazard maps  
536 generated for Hurricane Irma with the proposed curves and the Delft3D-FM model. The high  
537 accuracy of validation results ( $<0.2$  error) together with the rapid fashion of this approach for real-  
538 time flood hazard mapping suggests the proposed operative curves as a practical decision-making  
539 tool for on-time and reliable estimation of hazard areas in estuaries.

540



541 **Data availability**

542 All the data used in this study, including the gauge streamflow and water stage data are publicly  
543 available from the USGS and NOAA websites. The High Water Marks provided for Hurricanes  
544 Irma and Matthew are available from the USGS Flood Event Viewer platform.

545 **Author contribution**

546 KJafarzadegan and HMoradkhani conceptualized the study. KJafarzadegan designed the whole  
547 framework and implemented the hydrogeomorphic methodology. DMuñoz implemented the  
548 hydrodynamic modeling. KJafarzadegan and DMuñoz wrote the first draft of the manuscript.  
549 HMoradkhani, HMoftakhari a JGutenson, and GSavant provided comments and edited the  
550 manuscript.

551 **Competing interests**

552 The authors declare that they have no conflict of interest.

553

554 **Acknowledgment**

555 This work was financially supported by the USACE award # A20-0545-001. We would like to  
556 thank the anonymous reviewers for their constructive comments on the original version of the  
557 manuscript.

558

559



## 560 **References**

- 561 Afshari, S., Tavakoly, A. A., Rajib, M. A., Zheng, X., Follum, M. L., Omranian, E., and Fekete, B.  
562 M.: Comparison of new generation low-complexity flood inundation mapping tools with a  
563 hydrodynamic model, *J. Hydrol.*, 556, 539–556, <https://doi.org/10.1016/j.jhydrol.2017.11.036>,  
564 2018.
- 565 Alizad, K., Hagen, S. C., Medeiros, S. C., Bilskie, M. V., Morris, J. T., Balthis, L., and Buckel, C. A.:  
566 Dynamic responses and implications to coastal wetlands and the surrounding regions under sea  
567 level rise, *PLOS ONE*, 13, e0205176, <https://doi.org/10.1371/journal.pone.0205176>, 2018.
- 568 USGS Surface Water Information: <https://water.usgs.gov/osw/iwrss/>, last access: 16 November  
569 2021.
- 570 Arcement, G. J. and Schneider, V. R.: Guide for selecting Manning’s roughness coefficients for  
571 natural channels and flood plains, 1989.
- 572 Barbier, E. B.: Chapter 27 - The Value of Coastal Wetland Ecosystem Services, in: *Coastal*  
573 *Wetlands*, edited by: Perillo, G. M. E., Wolanski, E., Cahoon, D. R., and Hopkinson, C. S., Elsevier,  
574 947–964, <https://doi.org/10.1016/B978-0-444-63893-9.00027-7>, 2019.
- 575 Bass, B. and Bedient, P.: Surrogate modeling of joint flood risk across coastal watersheds, *J.*  
576 *Hydrol.*, 558, 159–173, <https://doi.org/10.1016/j.jhydrol.2018.01.014>, 2018.
- 577 Bates, P. D., Horritt, M. S., and Fewtrell, T. J.: A simple inertial formulation of the shallow water  
578 equations for efficient two-dimensional flood inundation modelling, *J. Hydrol.*, 387, 33–45,  
579 <https://doi.org/10.1016/j.jhydrol.2010.03.027>, 2010.
- 580 Bates, P. D., Quinn, N., Sampson, C., Smith, A., Wing, O., Sosa, J., Savage, J., Olcese, G., Neal, J.,  
581 Schumann, G., Giustarini, L., Coxon, G., Porter, J. R., Amodeo, M. F., Chu, Z., Lewis-Gruss, S.,  
582 Freeman, N. B., Houser, T., Delgado, M., Hamidi, A., Bolliger, I., E. McCusker, K., Emanuel, K.,  
583 Ferreira, C. M., Khalid, A., Haigh, I. D., Couasnon, A., E. Kopp, R., Hsiang, S., and Krajewski, W. F.:  
584 Combined Modeling of US Fluvial, Pluvial, and Coastal Flood Hazard Under Current and Future  
585 Climates, *Water Resour. Res.*, 57, e2020WR028673, <https://doi.org/10.1029/2020WR028673>,  
586 2021.
- 587 Chow Ven, T.: *Open channel hydraulics*, 1959.
- 588 Davidson, N. C.: How much wetland has the world lost? Long-term and recent trends in global  
589 wetland area, *Mar. Freshw. Res.*, 65, 934–941, <https://doi.org/10.1071/MF14173>, 2014.
- 590 Degiorgis, M., Gnecco, G., Gorni, S., Roth, G., Sanguineti, M., and Taramasso, A. C.: Classifiers  
591 for the detection of flood-prone areas using remote sensed elevation data, *J. Hydrol.*, 470–471,  
592 302–315, <https://doi.org/10.1016/j.jhydrol.2012.09.006>, 2012.



- 593 Degiorgis, M., Gnecco, G., Gorni, S., Roth, G., Sanguineti, M., and Taramasso, A. C.: Flood  
594 Hazard Assessment Via Threshold Binary Classifiers: Case Study of the Tanaro River Basin, *Irrig.  
595 Drain.*, 62, 1–10, <https://doi.org/10.1002/ird.1806>, 2013.
- 596 Dodov, B. A. and Fofoula-Georgiou, E.: Floodplain morphometry extraction from a high-  
597 resolution digital elevation model: a simple algorithm for regional analysis studies, *IEEE Geosci.  
598 Remote Sens. Lett.*, 3, 410–413, <https://doi.org/10.1109/LGRS.2006.874161>, 2006.
- 599 Eastern Research Group, Inc: Hurricane Forecast Improvement Program Socio-Economic  
600 Research and Recommendations:, NOAA National Weather Service, 2013.
- 601 Fagherazzi, S., Mariotti, G., Banks, A. T., Morgan, E. J., and Fulweiler, R. W.: The relationships  
602 among hydrodynamics, sediment distribution, and chlorophyll in a mesotidal estuary, *Estuar.  
603 Coast. Shelf Sci.*, 144, 54–64, <https://doi.org/10.1016/j.ecss.2014.04.003>, 2014.
- 604 Famikhilili, R., Talke, S. A., and Jay, D. A.: Tide-Storm Surge Interactions in Highly Altered  
605 Estuaries: How Channel Deepening Increases Surge Vulnerability, *J. Geophys. Res. Oceans*, 125,  
606 e2019JC015286, <https://doi.org/10.1029/2019JC015286>, 2020.
- 607 Fawcett, T.: An introduction to ROC analysis, *Pattern Recognit. Lett.*, 27, 861–874,  
608 <https://doi.org/10.1016/j.patrec.2005.10.010>, 2006.
- 609 Gharari, S., Hrachowitz, M., Fenicia, F., and Savenije, H. H. G.: Hydrological landscape  
610 classification: investigating the performance of HAND based landscape classifications in a  
611 central European meso-scale catchment, *Hydrol. Earth Syst. Sci.*, 15, 3275–3291,  
612 <https://doi.org/10.5194/hess-15-3275-2011>, 2011.
- 613 Gutenson, J.: A Review of Current and Future NWS Services, 2020.
- 614 Gutenson, J. L., Tavakoly, A. A., Massey, T. C., Savant, G., Tritinger, A. S., Owensby, M. B., Wahl,  
615 M. D., and Islam, M. S.: Investigating Modeling Strategies to Couple Inland Hydrology and  
616 Coastal Hydraulics to Better Understand Compound Flood Risk, 64–75,  
617 <https://doi.org/10.1061/9780784483466.006>, 2021.
- 618 Helton, J. C. and Davis, F. J.: Latin hypercube sampling and the propagation of uncertainty in  
619 analyses of complex systems, *Reliab. Eng. Syst. Saf.*, 81, 23–69, 2003.
- 620 IWRSS: Requirements for the National Flood Inundation Mapping Services, National Oceanic  
621 and Atmospheric Administration United States Army Corps of Engineers United States  
622 Geological Survey, 2013.
- 623 IWRSS: Design for the National Flood Inundation Mapping Services, National Oceanic and  
624 Atmospheric Administration United States Army Corps of Engineers United States Geological  
625 Survey, 2015.





- 626 Jafarzadegan, K. and Merwade, V.: A DEM-based approach for large-scale floodplain mapping in  
627 ungauged watersheds, *J. Hydrol.*, 550, 650–662, <https://doi.org/10.1016/j.jhydrol.2017.04.053>,  
628 2017.
- 629 Jafarzadegan, K. and Merwade, V.: Probabilistic floodplain mapping using HAND-based  
630 statistical approach, *Geomorphology*, 324, 48–61,  
631 <https://doi.org/10.1016/j.geomorph.2018.09.024>, 2019.
- 632 Jafarzadegan, K., Merwade, V., and Saksena, S.: A geomorphic approach to 100-year floodplain  
633 mapping for the Conterminous United States, *J. Hydrol.*, 561, 43–58,  
634 <https://doi.org/10.1016/j.jhydrol.2018.03.061>, 2018.
- 635 Jafarzadegan, K., Merwade, V., and Moradkhani, H.: Combining clustering and classification for  
636 the regionalization of environmental model parameters: Application to floodplain mapping in  
637 data-scarce regions, *Environ. Model. Softw.*, 125, 104613,  
638 <https://doi.org/10.1016/j.envsoft.2019.104613>, 2020.
- 639 Khojasteh, D., Chen, S., Felder, S., Heimhuber, V., and Glamore, W.: Estuarine tidal range  
640 dynamics under rising sea levels, *PLOS ONE*, 16, e0257538,  
641 <https://doi.org/10.1371/journal.pone.0257538>, 2021a.
- 642 Khojasteh, D., Glamore, W., Heimhuber, V., and Felder, S.: Sea level rise impacts on estuarine  
643 dynamics: A review, *Sci. Total Environ.*, 780, 146470,  
644 <https://doi.org/10.1016/j.scitotenv.2021.146470>, 2021b.
- 645 Kirwan, M. L. and Megonigal, J. P.: Tidal wetland stability in the face of human impacts and sea-  
646 level rise, *Nature*, 504, 53–60, <https://doi.org/10.1038/nature12856>, 2013.
- 647 Kulp, S. A. and Strauss, B. H.: New elevation data triple estimates of global vulnerability to sea-  
648 level rise and coastal flooding, *Nat. Commun.*, 10, 4844, <https://doi.org/10.1038/s41467-019-12808-z>, 2019.
- 650 Kumbier, K., Carvalho, R. C., Vafeidis, A. T., and Woodroffe, C. D.: Investigating compound  
651 flooding in an estuary using hydrodynamic modelling: a case study from the Shoalhaven River,  
652 Australia, *Nat. Hazards Earth Syst. Sci.*, 18, 463–477, <https://doi.org/10.5194/nhess-18-463-2018>, 2018.
- 654 Land, M., Tonderski, K., and Verhoeven, J. T. A.: Wetlands as Biogeochemical Hotspots Affecting  
655 Water Quality in Catchments, in: *Wetlands: Ecosystem Services, Restoration and Wise Use*,  
656 edited by: An, S. and Verhoeven, J. T. A., Springer International Publishing, Cham, 13–37,  
657 [https://doi.org/10.1007/978-3-030-14861-4\\_2](https://doi.org/10.1007/978-3-030-14861-4_2), 2019.
- 658 Liu, Z., Merwade, V., and Jafarzadegan, K.: Investigating the role of model structure and surface  
659 roughness in generating flood inundation extents using one-and two-dimensional hydraulic  
660 models, *J. Flood Risk Manag.*, 12, e12347, 2019.



- 661 Longenecker, H. E., Graeden, E., Kluskiewicz, D., Zuzak, C., Rozelle, J., and Aziz, A. L.: A rapid  
662 flood risk assessment method for response operations and nonsubject-matter-expert  
663 community planning, *J. Flood Risk Manag.*, 13, e12579, <https://doi.org/10.1111/jfr3.12579>,  
664 2020.
- 665 Luettich, R. A. (Richard A., Westerink, J. J., and Scheffner, N. W.: ADCIRC : an advanced three-  
666 dimensional circulation model for shelves, coasts, and estuaries. Report 1, Theory and  
667 methodology of ADCIRC-2DD1 and ADCIRC-3DL, This Digit. Resour. Was Creat. Scans Print  
668 Resour., 1992.
- 669 Maidment, D. R.: Conceptual Framework for the National Flood Interoperability Experiment,  
670 *JAWRA J. Am. Water Resour. Assoc.*, 53, 245–257, <https://doi.org/10.1111/1752-1688.12474>,  
671 2017.
- 672 Maidment, D. R., Clark, E., Hooper, R., and Ernest, A.: National Flood Interoperability  
673 Experiment, in: AGU Fall Meeting Abstracts, 2014.
- 674 Manfreda, S., Di Leo, M., and Sole, A.: Detection of Flood-Prone Areas Using Digital Elevation  
675 Models, *J. Hydrol. Eng.*, 16, 781–790, [https://doi.org/10.1061/\(ASCE\)HE.1943-5584.0000367](https://doi.org/10.1061/(ASCE)HE.1943-5584.0000367),  
676 2011.
- 677 Manfreda, S., Nardi, F., Samela, C., Grimaldi, S., Taramasso, A. C., Roth, G., and Sole, A.:  
678 Investigation on the use of geomorphic approaches for the delineation of flood prone areas, *J.*  
679 *Hydrol.*, 517, 863–876, <https://doi.org/10.1016/j.jhydrol.2014.06.009>, 2014.
- 680 Manfreda, S., Samela, C., Gioia, A., Consoli, G. G., Iacobellis, V., Giuzio, L., Cantisani, A., and  
681 Sole, A.: Flood-prone areas assessment using linear binary classifiers based on flood maps  
682 obtained from 1D and 2D hydraulic models, *Nat. Hazards*, 79, 735–754,  
683 <https://doi.org/10.1007/s11069-015-1869-5>, 2015a.
- 684 Manfreda, S., Samela, C., Gioia, A., Consoli, G. G., Iacobellis, V., Giuzio, L., Cantisani, A., and  
685 Sole, A.: Flood-prone areas assessment using linear binary classifiers based on flood maps  
686 obtained from 1D and 2D hydraulic models, *Nat. Hazards*, 79, 735–754,  
687 <https://doi.org/10.1007/s11069-015-1869-5>, 2015b.
- 688 McGlynn, B. L. and McDonnell, J. J.: Quantifying the relative contributions of riparian and  
689 hillslope zones to catchment runoff, *Water Resour. Res.*, 39,  
690 <https://doi.org/10.1029/2003WR002091>, 2003.
- 691 McGlynn, B. L. and Seibert, J.: Distributed assessment of contributing area and riparian  
692 buffering along stream networks, *Water Resour. Res.*, 39,  
693 <https://doi.org/10.1029/2002WR001521>, 2003.
- 694 McGrath, H., Bourgon, J.-F., Proulx-Bourque, J.-S., Nastev, M., and Abo El Ezz, A.: A comparison  
695 of simplified conceptual models for rapid web-based flood inundation mapping, *Nat. Hazards*,  
696 93, 905–920, <https://doi.org/10.1007/s11069-018-3331-y>, 2018.



- 697 Medeiros, S., Hagen, S., Weishampel, J., and Angelo, J.: Adjusting Lidar-Derived Digital Terrain  
698 Models in Coastal Marshes Based on Estimated Aboveground Biomass Density, *Remote Sens.*,  
699 7, 3507–3525, <https://doi.org/10.3390/rs70403507>, 2015.
- 700 Morton, R. A. and Barras, J. A.: Hurricane Impacts on Coastal Wetlands: A Half-Century Record  
701 of Storm-Generated Features from Southern Louisiana, *J. Coast. Res.*, 27, 27–43,  
702 <https://doi.org/10.2112/JCOASTRES-D-10-00185.1>, 2011.
- 703 Muis, S., Lin, N., Verlaan, M., Winsemius, H. C., Ward, P. J., and Aerts, J. C. J. H.: Spatiotemporal  
704 patterns of extreme sea levels along the western North-Atlantic coasts, *Sci. Rep.*, 9, 3391,  
705 <https://doi.org/10.1038/s41598-019-40157-w>, 2019.
- 706 Muñoz, D. F., Cissell, J. R., and Moftakhari, H.: Adjusting Emergent Herbaceous Wetland  
707 Elevation with Object-Based Image Analysis, Random Forest and the 2016 NLCD, *Remote Sens.*,  
708 11, 2346, <https://doi.org/10.3390/rs11202346>, 2019.
- 709 Muñoz, D. F., Moftakhari, H., and Moradkhani, H.: Compound effects of flood drivers and  
710 wetland elevation correction on coastal flood hazard assessment, *Water Resour. Res.*, 56,  
711 e2020WR027544, 2020.
- 712 Muñoz, D. F., Muñoz, P., Moftakhari, H., and Moradkhani, H.: From local to regional compound  
713 flood mapping with deep learning and data fusion techniques, *Sci. Total Environ.*, 782, 146927,  
714 2021.
- 715 Nardi, F., Vivoni, E. R., and Grimaldi, S.: Investigating a floodplain scaling relation using a  
716 hydrogeomorphic delineation method, *Water Resour. Res.*, 42,  
717 <https://doi.org/10.1029/2005WR004155>, 2006.
- 718 Roelvink, J. A. and Banning, G. K. F. M. V.: Design and development of DELFT3D and application  
719 to coastal morphodynamics, *Oceanogr. Lit. Rev.*, 11, 925, 1995.
- 720 Rogers, J. N., Parrish, C. E., Ward, L. G., and Burdick, D. M.: Improving salt marsh digital  
721 elevation model accuracy with full-waveform lidar and nonparametric predictive modeling,  
722 *Estuar. Coast. Shelf Sci.*, 202, 193–211, <https://doi.org/10.1016/j.ecss.2017.11.034>, 2018.
- 723 Samela, C., Manfreda, S., Paola, F. D., Giugni, M., Sole, A., and Fiorentino, M.: DEM-Based  
724 Approaches for the Delineation of Flood-Prone Areas in an Ungauged Basin in Africa, *J. Hydrol.*  
725 *Eng.*, 21, 06015010, [https://doi.org/10.1061/\(ASCE\)HE.1943-5584.0001272](https://doi.org/10.1061/(ASCE)HE.1943-5584.0001272), 2016.
- 726 Samela, C., Troy, T. J., and Manfreda, S.: Geomorphic classifiers for flood-prone areas  
727 delineation for data-scarce environments, *Adv. Water Resour.*, 102, 13–28,  
728 <https://doi.org/10.1016/j.advwatres.2017.01.007>, 2017.
- 729 Schieder, N. W., Walters, D. C., and Kirwan, M. L.: Massive Upland to Wetland Conversion  
730 Compensated for Historical Marsh Loss in Chesapeake Bay, USA, *Estuaries Coasts*, 41, 940–951,  
731 <https://doi.org/10.1007/s12237-017-0336-9>, 2018.



- 732 Sullivan, J. C., Torres, R., and Garrett, A.: Intertidal Creeks and Overmarsh Circulation in a Small  
733 Salt Marsh Basin, *J. Geophys. Res. Earth Surf.*, 124, 447–463,  
734 <https://doi.org/10.1029/2018JF004861>, 2019.
- 735 Teng, J., Vaze, J., Dutta, D., and Marvanek, S.: Rapid Inundation Modelling in Large Floodplains  
736 Using LiDAR DEM, *Water Resour. Manag.*, 29, 2619–2636, [https://doi.org/10.1007/s11269-015-](https://doi.org/10.1007/s11269-015-0960-8)  
737 [0960-8](https://doi.org/10.1007/s11269-015-0960-8), 2015.
- 738 Thomas, A., Dietrich, J., Asher, T., Bell, M., Blanton, B., Copeland, J., Cox, A., Dawson, C.,  
739 Fleming, J., and Luettich, R.: Influence of storm timing and forward speed on tides and storm  
740 surge during Hurricane Matthew, *Ocean Model.*, 137, 1–19,  
741 <https://doi.org/10.1016/j.ocemod.2019.03.004>, 2019.
- 742 Wamsley, T. V., Cialone, M. A., Smith, J. M., Atkinson, J. H., and Rosati, J. D.: The potential of  
743 wetlands in reducing storm surge, *Ocean Eng.*, 37, 59–68,  
744 <https://doi.org/10.1016/j.oceaneng.2009.07.018>, 2010.
- 745 Williams, W. A., Jensen, M. E., Winne, J. C., and Redmond, R. L.: An Automated Technique for  
746 Delineating and Characterizing Valley-Bottom Settings, in: *Monitoring Ecological Condition in*  
747 *the Western United States: Proceedings of the Fourth Symposium on the Environmental*  
748 *Monitoring and Assessment Program (EMAP), San Francisco, CA, April 6–8, 1999*, edited by:  
749 Sandhu, S. S., Melzian, B. D., Long, E. R., Whitford, W. G., and Walton, B. T., Springer  
750 Netherlands, Dordrecht, 105–114, [https://doi.org/10.1007/978-94-011-4343-1\\_10](https://doi.org/10.1007/978-94-011-4343-1_10), 2000.
- 751 Wing, O. E. J., Sampson, C. C., Bates, P. D., Quinn, N., Smith, A. M., and Neal, J. C.: A flood  
752 inundation forecast of Hurricane Harvey using a continental-scale 2D hydrodynamic model, *J.*  
753 *Hydrol. X*, 4, 100039, <https://doi.org/10.1016/j.hydroa.2019.100039>, 2019.
- 754 Wu, W., Zhou, Y., and Tian, B.: Coastal wetlands facing climate change and anthropogenic  
755 activities: A remote sensing analysis and modelling application, *Ocean Coast. Manag.*, 138, 1–  
756 10, <https://doi.org/10.1016/j.ocecoaman.2017.01.005>, 2017.
- 757 Zheng, X., Maidment, D. R., Tarboton, D. G., Liu, Y. Y., and Passalacqua, P.: GeoFlood: Large-  
758 Scale Flood Inundation Mapping Based on High-Resolution Terrain Analysis, *Water Resour. Res.*,  
759 54, 10,013–10,033, <https://doi.org/10.1029/2018WR023457>, 2018a.
- 760 Zheng, X., Tarboton, D. G., Maidment, D. R., Liu, Y. Y., and Passalacqua, P.: River Channel  
761 Geometry and Rating Curve Estimation Using Height above the Nearest Drainage, *JAWRA J. Am.*  
762 *Water Resour. Assoc.*, 54, 785–806, <https://doi.org/10.1111/1752-1688.12661>, 2018b.

763

764